

Original Research

# The VDAC3/DHODH Axis Ameliorates Sepsis-induced Myocardial Injury by Regulating Ferroptosis

Jiali Wang<sup>1,†</sup>, Fan Zhang<sup>1,†</sup>, Chaoqing Tan<sup>1</sup>, Nana Wang<sup>1</sup>, Xuexia Xia<sup>1,2</sup>, Yun Ye<sup>1</sup>, Yue Cao<sup>1</sup>, Xin Huang<sup>3</sup>, Zhenjiang Bai<sup>3</sup>, He Zhao<sup>4</sup>, Ling Sun<sup>1</sup>, Qiuqin Xu<sup>1</sup>, Huiting Zhou<sup>4,\*</sup>, Jie Huang<sup>1,\*</sup>

Academic Editor: Ioanna-Katerina Aggeli

Submitted: 6 April 2025 Revised: 16 May 2025 Accepted: 23 May 2025 Published: 17 June 2025

#### Abstract

Background: Sepsis-induced myocardial injury (SIMI) represents a major contributor to prolonged hospitalization in intensive care units (ICUs) and is associated with increased mortality rates. Mitochondria serve as the primary energy source for cardiomyocytes and are also essential for various other cell functions. The essential voltage-dependent anion channel 3 (VDAC3) protein located in the outer mitochondrial membrane plays a crucial role in preserving mitochondrial homeostasis by controlling metabolite transport and the shape of cristae. However, the precise mechanism by which VDAC3 is involved in SIMI remains unclear. This study aimed to explore the function and mechanism of VDAC3 in SIMI pathogenesis, with a particular emphasis on its regulatory role in ferroptosis. Methods: Lipopolysaccharide (LPS)-treated HL-1 cardiomyocytes (a murine cardiomyocyte cell line) were used to construct an in vitro myocardial injury model, and mice were used to establish a cecal ligation and puncture (CLP)-induced in vivo myocardial injury model. Transmission electron microscopy (TEM) was employed to evaluate the mitochondrial ultrastructure in cardiac tissues, while hematoxylin-eosin (H&E) staining was used to assess histopathological alterations. Echocardiography was used to evaluate the structural and functional characteristics of the heart. Integrated transcriptome and proteomic studies were performed to identify differentially expressed genes. VDAC3 expression levels, inflammatory responses, cellular proliferation, and ferroptosis were assessed using colorimetric assays, flow cytometry, enzyme-linked immunosorbent assay (ELISA), Cell Counting Kit-8 (CCK-8) proliferation assay, western blotting, and quantitative reverse transcription PCR (qRT-PCR). The relationship between VDAC3 and ferroptosis was investigated in vitro by transfecting cells with VDAC3 overexpression plasmids. Results: The injury model group in both the in vitro and in vivo experiments showed a decreased level of the antioxidant glutathione (GSH) and an elevated level of the lipid peroxidation product malondialdehyde (MDA). Moreover, ferroptosis regulation occurred through the modulation of glutathione peroxidase 4 (GPX4), solute carrier family 7 members 11 (SLC7A11), ferritin, prostaglandin-endoperoxide synthase 2 (PTGS2), lipocalin 2 (LCN2), and acyl-coenzyme A (CoA)-synthetase long-chain family member 4 (ACSL4) expression. Administration of ferrostatin-1 (Fer-1), an inhibitor of ferroptosis, markedly reduced the cardiac injury caused by CLP. Additionally, VDAC3 expression was significantly downregulated in experimental models and septic children. In contrast, Fer-1 treatment increased the expression of both VDAC3 and dihydroorotate dehydrogenase (DHODH) and significantly ameliorated cardiac damage. Overexpression of VDAC3 reduced mitochondrial oxidative stress, increased the expression of DHODH, and altered the progression of ferroptosis. Conclusion: Collectively, this research provides insights into the molecular mechanism behind the VDAC3/DHODH axis in SIMI. This axis mitigates cardiac injury by regulating ferroptosis, thereby suggesting novel therapies for SIMI.

Keywords: VDAC3; DHODH; ferroptosis; mitochondria; sepsis; myocardial injury

#### 1. Introduction

Sepsis occurs because of a dysregulated host response to infection, leading to potentially lethal organ failure that is characterized by complicated physiological, pathophysiological, and biochemical processes [1,2]. Sepsis-related multi-organ dysfunction is a major cause of patient death in intensive care units (ICUs), as well as elevating the cost of healthcare [3]. Septic shock is a subset of sepsis char-

acterized by concurrent circulatory, cellular, and metabolic dysfunction. It is also associated with a significantly higher mortality risk compared to sepsis without shock [4]. Sepsis-induced myocardial injury (SIMI), defined as reversible myocardial dysfunction, typically manifests in patients with sepsis, and particularly those progressing to septic shock [5]. Clinical data reveal a 20% mortality rate in septic patients without myocardial involvement, versus 70–90%

<sup>&</sup>lt;sup>1</sup>Department of Cardiology, Children's Hospital of Soochow University, 215003 Suzhou, Jiangsu, China

<sup>&</sup>lt;sup>2</sup>Department of Pediatrics, Wuxi Ninth People's Hospital Affiliated to Soochow University, 215003 Wuxi, Jiangsu, China

<sup>&</sup>lt;sup>3</sup>Pediatric Intensive Care Unit, Children's Hospital of Soochow University, 215003 Suzhou, Jiangsu, China

<sup>&</sup>lt;sup>4</sup>Institute of Pediatric Research, Children's Hospital of Soochow University, 215003 Suzhou, Jiangsu, China

<sup>\*</sup>Correspondence: huitingzhousdfey@163.com (Huiting Zhou); j.shuang@163.com (Jie Huang)

<sup>†</sup>These authors contributed equally.

in those with SIMI [6]. Although considered to be a reversible complication, SIMI is associated with poor clinical outcomes, with a reported hospitalization rate of 35% and 1-year mortality rate of 51% in affected patients [7]. Emerging evidence highlights the critical role of mitochondrial dysfunction in SIMI pathogenesis [8,9]. Mitochondria are central regulators of myocardial energy metabolism and integrate multiple metabolic pathways, thus making them key mediators in this pathological process [10].

Cardiac energy metabolism relies predominantly on lipid pathways for adenosine triphosphate (ATP) generation. Approximately 60~90% of myocardial ATP production is derived from  $\beta$ -oxidation of fatty acids, with the remaining ATP synthesis derived from oxidation of glucose, lactate, ketone bodies, and amino acids [11]. Ferroptosis is a distinct iron-dependent form of regulated cell death characterized by lethal lipid peroxide accumulation. It is characterized by unique biochemical, morphological, and regulatory mechanisms compared to apoptosis, autophagy, and necroptosis [12,13]. This cell death modality has gained significant attention in preclinical research due to its involvement in various pathological conditions. Ferroptosis is also primarily a process that balances oxidative and antioxidant damage [14]. Its development is mechanistically linked to glutathione depletion and to inactivation of glutathione peroxidase 4 (GPX4), which are key components of the cellular antioxidant system [15]. In addition, shortterm lactate stimulation activates mitochondrial and oxidative stress processes to induce mitochondrial-dependent ferroptosis [16]. Notably, cells undergoing ferroptosis can release damage-related molecular patterns (DAMPs) and undergo lipid peroxidation, thereby mediating inflammatory responses that exacerbate sepsis-induced multiorgan dysfunction [17,18].

Cardiac tissues demonstrate a marked susceptibility to oxidative damage, with lipid peroxidation serving as a critical pathological mediator in reactive oxygen species (ROS)-induced cardiac injury. Multiple endogenous ROS generation pathways exist in cardiac tissues, including but not limited to the mitochondrial electron transport chain, nicotinamide adenine dinucleotide phosphate (NADPH) oxidase, xanthine oxidoreductase, nitric oxide synthase, and cytochrome P450 enzymatic complexes [19]. Emerging experimental evidence highlights the central role of mitochondria in the pathogenesis of ferroptosis [20]. Ultrastructural changes occur in the mitochondria during ferroptosis, including mitochondrial contraction and cristae fragmentation. Impaired mitochondrial dynamics and dysfunction significantly increase the susceptibility to ferroptosis [12].

The calcium transfer-mitochondrial ROS axis and the lipid transfer-polyunsaturated fatty acid-containing triacylglycerol axis are both controlled by the mitochondrial membrane and are critically involved in the execution of ferroptosis [21]. Voltage dependent anion channels (VDACs),

also known as mitochondrial pore proteins, are the most abundant outer mitochondrial membrane (OMM) proteins that mediate metabolite transport between the mitochondria and cytoplasm [22,23]. Of the three VDAC isoforms, VDAC1 and VDAC2 are co-localized in distinct domains of the OMM, whereas VDAC3 is more broadly distributed across this membrane [24]. Notably, the VDAC3 promoter shows enrichment for several specific motifs required for the mitochondrial stress response [25]. VDAC3 cysteine has a key role in the regulation of mitochondrial ROS [26]. Functionally, VDAC3 is involved in recruiting PTEN-induced kinase 1 (PIK1), a cytoplasmic protein essential for mitochondrial quality control by regulating the selective autophagic clearance of depolarized mitochondria [27]. Emerging studies have confirmed the involvement of VDAC3 in modulating ferroptosis via distinct molecular pathways [28–30]. However, it remains to be elucidated whether VDAC3 regulates ferroptosis in the pathogenesis of SIMI.

The analysis of global metabolomics data in 2021 revealed a novel mitochondrial defense mechanism against ferroptosis. Mitochondrial dihydroorotate dehydrogenase (DHODH) and mitochondrial GPX4 act as critical regulators of mitochondrial lipid peroxidation [31]. DHODH is located in the inner mitochondrial membrane (IMM) and serves as the rate-limiting enzyme in the de novo pyrimidine nucleotide synthesis pathway [32]. This multifunctional therapeutic target has demonstrated clinical relevance across various pathological conditions. Due to the critical role of de novo pyrimidine nucleotide biosynthesis in tumor growth, DHODH inhibitors have been investigated for possible treatment of cancer [33]. Furthermore, pharmacological modulation of DHODH has shown promise in ameliorating ovariectomy-induced cognitive decline [34]. However, the mechanism involving DHODH in SIMI remains unclear, with further investigations required to fully explore its role.

We therefore established a murine model of SIMI through cecal ligation and puncture (CLP), and also developed a lipopolysaccharide (LPS)-induced HL-1 cardiomyocyte model. In addition, we collected serum samples from septic patients in order to investigate the functional role of the VDAC3/DHODH axis and its underlying mechanism in SIMI pathogenesis, with the aim of identifying novel therapeutic targets for SIMI.

#### 2. Materials and Methods

#### 2.1 Clinical Ethics and Patients

This study enrolled 29 pediatric patients diagnosed with sepsis (Sepsis group) and 29 healthy children (Healthy group) hospitalized at the Children's Hospital of Soochow University from April 2024 to December 2024. Clinical samples and data were collected after written informed consent was obtained from the guardians of all participants. The study protocol was reviewed and approved by the Med-



Table 1. Experimental groups and procedures.

| Group        | Procedure   |
|--------------|---|
| CLP          | Induced by CLP to establish polymicrobial sepsis-induced myocardial injury                          |
| sham         | Laparotomy and closure only   |
| sham + Fer-1 | Laparotomy and closure, followed by intraperitoneal injection of 5 mg/kg Fer-1 at 2 h post-surgery  |
| sham + PBS   | Laparotomy and closure, followed by intraperitoneal injection of equivalent PBS at 2 h post-surgery |
| CLP + Fer-1  | CLP-induced sepsis with intraperitoneal injection of 5 mg/kg Fer-1 at 2 h post-surgery              |
| CLP + PBS    | CLP-induced sepsis with intraperitoneal injection of equivalent PBS at 2 h post-surgery             |

Note: Fer-1, ferrostatin-1; CLP, cecal ligation and puncture; PBS, phosphate-buffered saline. Fer-1 was administered at a dose of 5 mg/kg as described previously [35].

ical Ethics Committee of the Children's Hospital of Soochow University (2024CS169).

#### 2.2 Mice

Male C57BL/6J mice (specific pathogen free grade, 7~8 weeks old, 20~24 g) were purchased from Hangzhou Ziyuan Laboratory Animal Technology Co., Ltd. [SCXK (Zhe) 2024-0004]. The mice were acclimatized under controlled environmental conditions at an ambient temperature of 22~28 °C, relative humidity of 50%, and 12 h/12 h day/night alternation. All animal experiments met the requirements of the Animal Experimentation and Ethics Committee of Soochow University (SUDA20241104A02). The 3R principle was followed throughout the experimental process.

#### 2.3 CLP Sepsis Model

A murine model of polymicrobial SIMI was established by performing CLP using established protocols [9]. Briefly, Anesthesia was induced in C57BL/6 mice via inhalation of 2.5% isoflurane and maintained with 1% isoflurane. Then the mice were placed in a supine position on the surgical platform. The limbs were fixed with adhesive tape, the abdomen was prepared and disinfected with iodine povidone, and a median incision of about 1 cm in length was made along the white line of the abdomen. The abdominal musculature was bluntly separated and the cecum exposed and carefully separated, avoiding damage to the blood vessels. Its contents were then squeezed to the distal end, and the cecum ligated with a sterile 4-gauge wire at one-third of the distance from the blind end. The distal end of the ligation was perforated with a 22G needle. The cecum was then returned to the abdominal cavity and the abdomen closed after squeezing out a small amount of intestinal content. Careful attention was paid throughout the operation to avoid injury to blood vessels and organ tissues. Immediately after surgery, 1 mL of preheated saline was injected subcutaneously and the mice were placed on a thermostatic electric blanket and returned to their cage after awakening. Sham-operated controls underwent identical anesthesia and laparotomy procedures without cecal manipulation, followed by equivalent saline resuscitation.

The mice were randomly divided into 6 groups, as

shown in Table 1 (Ref. [35]): sham, CLP, sham + PBS, sham + Fer-1, CLP + PBS, and CLP + Fer-1.

#### 2.4 Collection of Mouse Samples

Samples were collected 24 h post-modeling based on previous work [36] and preliminary experimental results. At the designated time point, the mice were anaesthetized using 2.5% isoflurane inhalation, and an appropriate amount of whole blood was collected. Serum was separated by centrifugation and stored at -80 °C for subsequent analysis. After blood collection, the mice were sacrificed by cervical dislocation, and the cardiac tissues were harvested. The thoracic cavity was surgically exposed by partial sternal and costal resection after limb fixation. The intact heart was carefully excised using blunt dissection techniques and immediately rinsed with pre-cooled PBS (Servicebio, Cat# G4202, Wuhan, China) to remove residual blood. The harvested organs were temporarily maintained in 1.5 mL microcentrifuge tubes on ice, with particular attention paid to minimizing mechanical trauma during surgical manipulation. The collected cardiac tissues were used for transcriptomics and proteomics sequencing analyses, histopathological evaluation, and HT7800/HT7700 transmission electron microscopy (HITACHI, Tokyo, Japan) observation. Any remaining aliquots were cryopreserved at −80 °C for potential future investigations.

#### 2.5 HL-1 Cardiomyocytes

HL-1 cardiomyocytes were purchased from HyCyte (Suzhou, China) and cultured in complete growth medium under standard incubator conditions. They were then passaged or used in subsequent experiments according to the growth density and status of the cells. Based on the methodology described in reference [37] and confirmed by preliminary experiments, the *in vitro* myocardial injury model was established by stimulating cells with 1 μg/mL LPS (Sigma, Cat# L5293, Shanghai, China). The cell line was validated by short tandem repeat (STR) profiling and tested negative for mycoplasma.

#### 2.6 Cell Transfection

The overexpression plasmids used in this study were constructed by GenePharma (Suzhou, China). HL-1 car-



diomyocytes in the logarithmic growth phase were seeded into 24-well plates and transfected with the plasmids after reaching 60–80% confluence. The GP-transfect-Mate transfection reagent (GenePharma, Suzhou, China) was used as recommended by the manufacturer, and the efficiency of transfection was assessed quantitatively by fluorescence microscopy (OLYMPUS, Tokyo, Japan) after 24 h

#### 2.7 RNA Sequencing

Serum samples were collected from the CLP model in mice to quantify myocardial injury biomarkers, including creatine kinase-MB isoenzyme (CK-MB) and cardiac troponin T (cTnT). Cardiac tissues from CLP model mice exhibiting significant myocardial injury were subsequently submitted to Novogene for transcriptome sequencing, together with their sham-operated counterparts. Differentially expressed genes (DEGs) were identified using the DESeq2 1.42.0 in R 4.3.2 software (https://cloud.r-project.org/bin/), with three biological replicates per group. The selection criteria for DEGs were set as  $|\log 2(\text{Fold-Change})| \ge 0.25$  and p-value  $\le 0.05$ . A heatmap to visualize the clustering of DEGs across different experimental groups was generated using the pheatmap 1.0.12 (https://cran.r-project.org/web/packages/pheatmap/).

#### 2.8 Proteome Sequencing

Following establishment of the model, cardiac tissue samples from both the myocardial injury model group and the sham-operated group were selected based on the serum levels of CK-MB and cTnT. These were submitted to PTM BIO (Hangzhou, China) for proteomic sequencing analysis. Differentially expressed proteins (DEPs) were identified using the stringent criteria of a  $|\text{Log2}(\text{Fold-Change})| \ge 1.5$  and  $p\text{-value} \le 0.05$ . Proteomic data were visualized using a heatmap, and functional enrichment analyses including Kyoto Encyclopedia of Genes and Genomes (KEGG) and Gene ontology (GO) classification were performed. KEGG results were presented in chord diagram format, while GO enrichment results were displayed as bar graphs, ensuring comprehensive visualization of the analytical results.

#### 2.9 Transmission Electron Microscopy (TEM)

Fresh murine cardiac tissue specimens were collected and dissected into fragments of approximately one mm<sup>3</sup>. The tissue samples were immediately immersed in electron microscopy-grade, glutaraldehyde-based fixative (Servicebio, Cat# G1102, Wuhan, China) for primary fixation. This initial fixation was performed under light-protected conditions at room temperature for 2 h, followed by storage at 4 °C to maintain ultrastructural integrity. All fixed specimens were subsequently transferred to Servicebio (Wuhan, China) for further processing and ultrastructural analysis using standardized HT7800/HT7700 TEM (HITACHI, Tokyo, Japan) protocols.

### 2.10 Detection of Malondialdehyde (MDA) and Glutathione

The total glutathione content, reduced glutathione (GSH) level, and GSH/oxidized glutathione (GSSG) ratio in cardiac tissues and HL-1 cardiomyocytes were quantitatively analyzed using a GSH/GSSG assay kit (Beyotime, Cat# S0053, Shanghai, China) as recommended by the manufacturer. The level of malondialdehyde (MDA), a lipid peroxidation biomarker, was simultaneously determined using an MDA assay kit (Beyotime, Cat# S0131S, Shanghai, China) as recommended by the manufacturer. To ensure accurate comparative analysis, the final concentrations of MDA and GSH were normalized to the total protein content measured in corresponding tissue homogenates or cellular lysates.

#### 2.11 Western Blotting

Total protein was extracted from cardiac tissue and cultured cells using RIPA lysis buffer (Beyotime, Cat# P0013C). Protein samples were separated by SDS-PAGE electrophoresis and subsequently transferred onto PVDF membranes (Millipore, Boston, MA, USA). After blocking with 5% BSA (Biosharp, Hefei, China) for 2 h at room temperature, the membranes underwent sequential incubations with the primary antibodies listed in Table 2, followed by the corresponding horseradish peroxidase-conjugated secondary antibodies. Membranes were incubated overnight at 4 °C with primary antibodies, followed by three washes with Tris-buffered saline with Tween®-20 (TBST) (Fudebio, Hangzhou, China) and then an 1 h incubation at room temperature with secondary antibody. Protein bands were visualized using enhanced chemiluminescence detection reagents (Fudebio, Hangzhou, China) and quantitatively analyzed with ImageJ software (version Fiji; National Institute of Health, Bethesda, MD, USA).

#### 2.12 Quantitative Real-time PCR (qRT-PCR)

Total RNA was isolated from cardiac tissues and cultured cells using an RNA extractor (BBI, Cat# B610409-0100, Shanghai, China). The RNA concentration and purity were determined based on spectrophotometric measurements. Subsequently, RNA samples were reversetranscribed into complementary DNA (cDNA) using 5× All-In-One RT MasterMix (ABM, Cat# G490, Zhenjiang, China) as recommended by the manufacturer. The cDNA was used as a template for PCR amplification with the SYBR Green Pro Taq HS Premixed qPCR kit (Accurate Biology, Cat# AG11701, Changsha, China). Relative expression levels were calculated using the  $2^{-\Delta\Delta Ct}$  method and normalized to  $\beta$ -actin. All primer sequences were synthesized commercially by ATANTARES (Suzhou, China), with the reaction specificity confirmed through melting curve analysis. The primer sequences are shown in Table 3.



Table 2. Antibody details.

|                                | •        |               |
|--------------------------------|----------|---------------|
| Antibody                       | Source   | Identifier    |
| Anti-VDAC3                     | ABclonal | Cat# A10544   |
| Anti-DHODH                     | Abcam    | Cat# ab174288 |
| Anti-GAPDH                     | Abcam    | Cat# ab8245   |
| Anti-SLC7A11                   | Abmart   | Cat# T57046S  |
| Anti-GPX4                      | Abcam    | Cat# ab125066 |
| Anti-Ferritin                  | Abmart   | Cat# T55648F  |
| Goat anti-rabbit IgG (H&L) HRP | Fudebio  | Cat# FDR007   |
|                                |          |               |

Note: VDAC3, voltage-dependent anion channel 3; DHODH, dihydroorotate dehydrogenase; GAPDH, glyceraldehyde-3-phosphate dehydrogenase; SLC7A11, solute carrier family 7 members 11; GPX4, glutathione peroxidase 4.

Table 3. Primer sequences for qRT-PCR.

|                 |         | <u> </u>                      |
|-----------------|---------|-------------------------------|
| Mouse genes     |         | Sequence                      |
| VDAC3           | Forward | 5'-GACGGGATTGTTTTAGTCTCGG-3'  |
|                 | Reverse | 5'-GCCTTGTAACCAAGAGCGAAA-3'   |
| DHODH           | Forward | 5'-TTCACCTCTTACCTGACAGCC-3'   |
|                 | Reverse | 5'-TGGAGTCCTGAAACGTAGCTC-3'   |
| GPX4            | Forward | 5'-TGTGCATCCCGCGATGATT-3'     |
|                 | Reverse | 5'-CCCTGTACTTATCCAGGCAGA-3'   |
| SLC7A11         | Forward | 5'-GGCACCGTCATCGGATCAG-3'     |
|                 | Reverse | 5'-CTCCACAGGCAGACCAGAAAA-3'   |
| PTGS2           | Forward | 5'-TGCACTATGGTTACAAAAGCTGG-3' |
|                 | Reverse | 5'-TCAGGAAGCTCCTTATTTCCCTT-3' |
| LCN2            | Forward | 5'-GCAGGTGGTACGTTGTGGG-3'     |
|                 | Reverse | 5'-CTCTTGTAGCTCATAGATGGTGC-3' |
| IL-6            | Forward | 5'-CTGCAAGAGACTTCCATCCAG-3'   |
|                 | Reverse | 5'-AGTGGTATAGACAGGTCTGTTGG-3' |
| $IL$ - $1\beta$ | Forward | 5'-GAAATGCCACCTTTTGACAGTG-3'  |
|                 | Reverse | 5'-TGGATGCTCTCATCAGGACAG-3'   |
| $\beta$ -actin  | Forward | 5'-GGCTGTATTCCCCTCCATCG-3'    |
|                 | Reverse | 5'-CCAGTTGGTAACAATGCCATGT-3'  |

Note: PTGS2, prostaglandin peroxidase synthase 2; LCN2, lipocalin 2; IL-6, interleukin-6; IL-1 $\beta$ , interleukin-1 $\beta$ ; qRT-PCR, quantitative reverse transcription PCR.

#### 2.13 Enzyme-linked Immunosorbent Assay (ELISA)

Levels of the tumor necrosis factor- $\alpha$  (TNF- $\alpha$ ) and IL-6 in mouse serum and cell culture supernatant were measured using mouse TNF- $\alpha$  and IL-6 ELISA kits (Dakewe, Cat# 1217202, Cat# 1210602, Shanghai, China) as recommended by the manufacturer. The myocardial injury biomarkers cTnT and CK-MB in mouse serum were quantified using corresponding mouse ELISA kits (Elabscience, Cat# E-EL-M0355, Cat# E-EL-M1801, Wuhan, China) according to standard protocols. Human VDAC3 levels in patient serum were evaluated using the human VDAC3 ELISA kit (EYKITS, Cat# EY-k836117, Shanghai, China) as recommended by the manufacturer.

#### 2.14 Echocardiography Evaluation

Anesthesia was induced in mice using 2.5% isoflurane inhalation, followed by maintenance with 1% isoflurane until completion of the examination. After anesthesia, mice were placed in a supine posture and secured at the center of a heating pad. Depilatory cream was then applied evenly to the thoracic region using cotton swabs. After 2~3 minutes, the cream was thoroughly removed using clean cotton swabs. Ultrasound gel was uniformly applied to the transducer contact area, and transthoracic echocardiography was performed to evaluate cardiac structural and functional alterations.



#### 2.15 Hematoxylin-eosin (H&E) Staining

Following paraffin embedding of the mouse heart, 4 µm tissue sections were prepared for H&E (Servicebio, Cat# G1076, Wuhan, China) staining as previously described [38]. Briefly, mouse cardiac tissues were fixed in 4% paraformaldehyde (Servicebio, Cat# G1101, Wuhan, China) solution and then subjected sequentially to dehydration, transparency, wax dipping, embedding, sectioning, dewaxing, dehydration, rinsing, and H&E staining. This was followed by dehydration, clearing, and mounting. The sections were then observed by light microscopy and the images recorded.

#### 2.16 Evaluation of Lipid Peroxidation by Flow Cytometry

Cardiomyocytes in good growth condition were uniformly seeded into 6-well plates and grown in a cell culture incubator. After reaching 60–80% confluency, the cells were transfected with a VDAC3-overexpression plasmid for 24 h and then stimulated with 1 µg/mL LPS for 6 h. Subsequently, they were harvested after digestion and centrifuged at 600 g for 5 min. The supernatant was discarded and cellular lipid peroxidation was measured using the Lipid Peroxidation assay kit with BODIPY 581/591 C11 (Beyotime, Cat# S0043S) as recommended by the manufacturer. Briefly, 2  $\mu$ M BODIPY 581/591 C11 was incubated with cells at 37 °C for 30 min, washed twice with  $1\times$  PBS and then analyzed by flow cytometry. Data analysis was performed using FlowJo 10.8 (FlowJo, LLC, Ashland, OR, USA).

#### 2.17 Cell Viability Assay

Cardiomyocytes in good growth condition were uniformly seeded into 96-well plates and grown in a cell culture incubator. After reaching 60–80% confluency, the cells were transfected with VDAC3-overexpression plasmid (GenePharma, Suzhou, China) for 24 h. Cell viability was measured at 0, 24, 48, and 72 h post-transfection using the CCK-8 kit (Fudebio, Cat# FD3788, Hangzhou, China). Cells were incubated with 100  $\mu L/well$  CCK-8 reagent (Fudebio, Cat# FD3788, Hangzhou, China) for 1.5 h and the absorbance measured at 450 nm using an enzyme marker (Thermo, Waltham, MA, USA).

#### 2.18 ROS Detection

Cardiomyocytes in good growth condition were uniformly seeded into 24-well plates and grown in a cell culture incubator. After reaching 60–80% confluency, the cells were transfected with VDAC3-overexpression plasmid for 24 h, followed by stimulation with 1  $\mu$ g/mL LPS for 6 h. Cellular ROS levels were measured using the ROS assay kit (Beyotime, Cat# S0033S) and Hoechst 33342 Staining Solution for Live Cells (Beyotime, Cat# C1027) as recommended by the manufacturer. Briefly, cells were incubated with 10  $\mu$ M DCFH-DA and 1 $\times$  Hoechst stain for 20 min, washed three times, and then imaged using fluorescence mi-

croscopy [39]. Data analysis was performed using ImageJ software.

#### 2.19 Statistical Analysis

Statistical analyses were performed using GraphPad Prism 8 software (GraphPad Software Inc., San Diego, CA, USA). Normally distributed continuous data were expressed as the mean  $\pm$  standard deviation (mean  $\pm$  SD). Comparisons between two groups were conducted using unpaired two-tailed Student's *t*-tests. Multiple group comparisons were analyzed using one-way analysis of variance (ANOVA) with Tukey's post hoc test, or two-way ANOVA with Sidak's multiple comparisons test. Relationships between continuous variables were assessed using Spearman's rank correlation coefficient. The number of biological replicates (n) for each experiment is specified in the corresponding figure legends. A *p* value of <0.05 was considered to represent statistical significance.

#### 3. Results

# 3.1 Ferrostatin-1 (Fer-1) Significantly Inhibited CLP-induced Ferroptosis

To investigate the role of ferroptosis in CLP-induced myocardial injury, we established a SIMI mouse model as described in the Methods and then administered 5 mg/kg of Fer-1. TEM analysis revealed distinct ultrastructural changes in the mitochondria. Myocardial cells in both the Sham+PBS and Sham+Fer-1 groups exhibited well-organized mitochondrial arrays with intact membranes, uniform matrix density, and well-preserved cristae (Fig. 1A). In contrast, the CLP+PBS group displayed marked mitochondrial disorganization characterized by swelling, vacuolization, membrane rupture with increased electron density, and fragmentation or loss of cristae. Notably, Fer-1 treatment in the CLP+Fer-1 group substantially ameliorated these pathological alterations.

The colorimetric assay results for oxidative stress levels in the cardiac tissues of mice revealed no significant differences between the Sham+PBS and Sham+Fer-1 groups in terms of total glutathione content, GSH, and GSH/GSSG ratio (Fig. 1C–E). However, the CLP+PBS group exhibited significantly decreased total glutathione, GSH, and GSH/GSSG ratio, accompanied by a marked increase in the lipid peroxidation metabolite MDA (Fig. 1B). Administration of Fer-1 in the CLP+Fer-1 group significantly increased the total glutathione, GSH, and GSH/GSSG ratio compared to the CLP+PBS group, while simultaneously reducing the MDA level (Fig. 1B–E). Collectively, these findings indicate that Fer-1 can effectively suppress CLP-induced oxidative stress.

Western blot analysis of ferroptosis-related proteins (Fig. 1F) revealed no significant differences in myocardial ferritin, GPX4, and solute carrier family 7 members 11 (SLC7A11) protein levels between the Sham+PBS and Sham+Fer-1 groups (Fig. 1G–I). In contrast, the



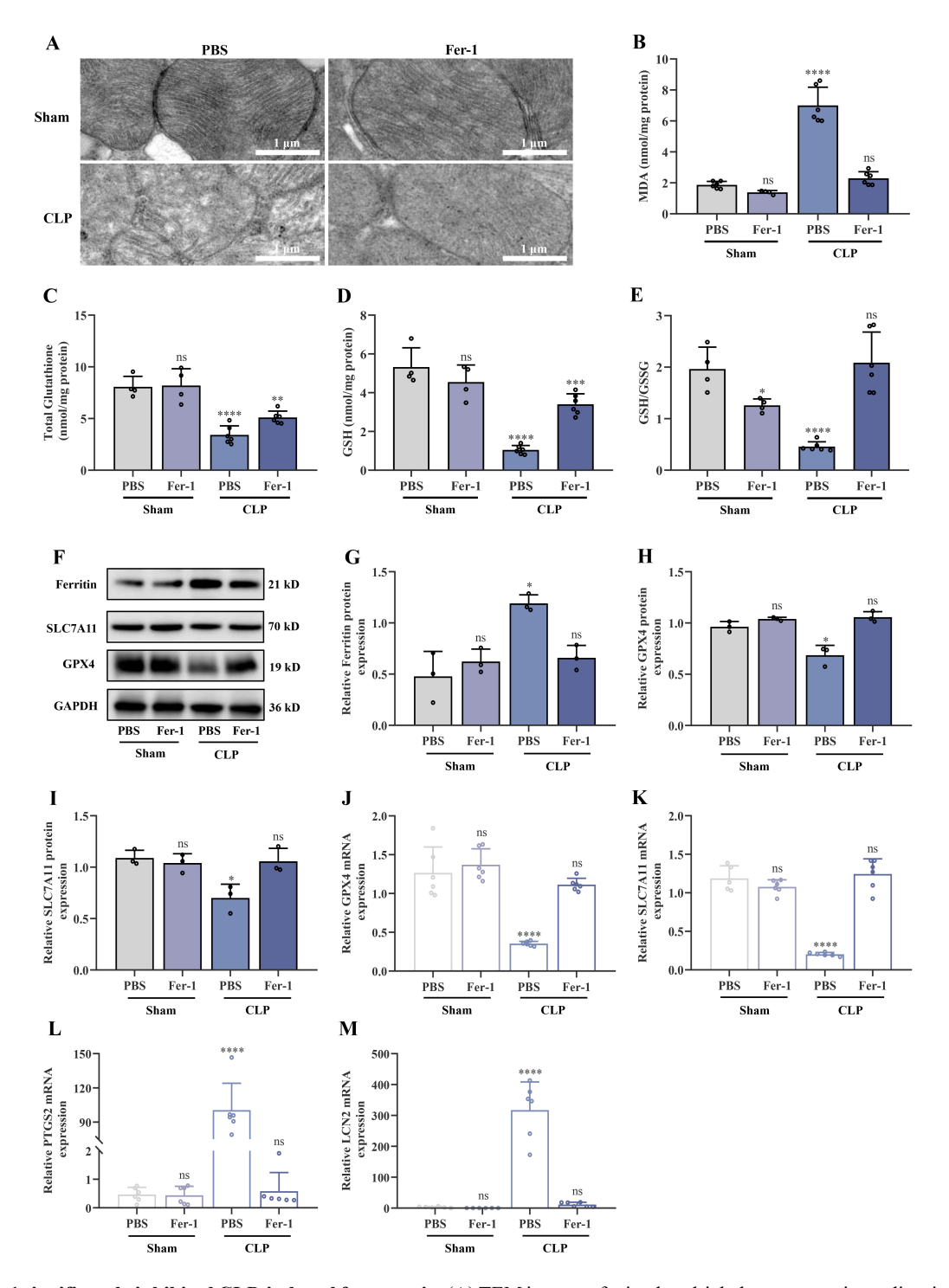


Fig. 1. Fer-1 significantly inhibited CLP-induced ferroptosis. (A) TEM images of mitochondrial ultrastructure in cardiac tissues (Scale bar = 1  $\mu$ m; n = 5). (B) MDA levels in cardiac tissues (n = 6). (C–E) Glutathione profiles in cardiac tissues (n = 6): total glutathione (C), GSH (D), and GSH/GSSG ratio (E). (F) Western blot showing protein expression of ferroptosis-related markers in cardiac tissues (n = 3): ferritin quantification (G), GPX4 quantification (H), and SLC7A11 quantification (I). qRT-PCR showing relative mRNA expression in cardiac tissues (n = 6): GPX4 (J), SLC7A11 (K), PTGS2 (L), and LCN2 (M). Data are expressed as the mean  $\pm$  SD. Statistical analyses were performed using one-way ANOVA with Tukey's multiple comparisons test. \*p < 0.05, \*\*\*p < 0.01, \*\*\*\* p < 0.001, \*\*\*\* p < 0.0001, ns p > 0.05. Abbreviations: TEM, transmission electron microscopy; MDA, malondialdehyde; GSH, reduced glutathione; GSSG, oxidized glutathione; GPX4, glutathione peroxidase 4; SLC7A11, solute carrier family 7 member 11; PTGS2, prostaglandinendoperoxide synthase 2; LCN2, lipocalin 2; Fer-1, Ferrostatin-1; CLP, cecal ligation and puncture; SD, standard deviation.

CLP+PBS group exhibited significantly decreased GPX4 and SLC7A11 protein expression (Fig. 1H,I), but markedly increased ferritin expression (Fig. 1G). Fer-1 treatment effectively reversed these alterations in the CLP+Fer-1 group by restoring GPX4 and SLC7A11 expression, while reducing ferritin to levels comparable with the CLP+PBS group. qRT-PCR analysis of mRNA expression revealed similar regulatory effects (Fig. 1J-M). No significant differences in PTGS2, LCN2, GPX4, or SLC7A11 mRNA levels were observed between the Sham+PBS and Sham+Fer-1 groups. However, the CLP+PBS group showed significant downregulation of the GPX4 and SLC7A11 transcripts (Fig. 1J,K), accompanied by substantial upregulation of PTGS2 and LCN2 mRNA (Fig. 1L,M). Following Fer-1 treatment, mouse cardiac tissue from the CLP+Fer-1 group showed significantly increased expression of GPX4 and SLC7A11 mRNA compared to the CLP+PBS group, but markedly reduced expression of PTGS2 and LCN2 mRNA.

Taken together, these findings demonstrate that intraperitoneal administration of Fer-1 effectively inhibited CLP-induced ferroptosis through coordinated regulation of key ferroptosis-related markers at both the protein and mRNA levels.

### 3.2 Inhibition of Ferroptosis Effectively Improved CLP-induced Myocardial Injury

To further investigate the relationship between ferroptosis and myocardial injury, we examined whether Fer-1 treatment could ameliorate myocardial damage. ELISA assays revealed there were no significant differences between the Sham+Fer-1 and Sham+PBS groups in the serum levels of pro-inflammatory cytokines IL-6 and TNF- $\alpha$ . In contrast, the CLP+PBS group showed markedly elevated levels of IL-6 and TNF- $\alpha$  relative to the Sham+PBS group. Notably, Fer-1 treatment significantly reduced the levels of these inflammatory mediators in the CLP+Fer-1 group compared to the CLP+PBS group, although no significant differences were observed between the CLP+Fer-1 and Sham+PBS groups (Fig. 2A,B). These findings suggest that Fer-1 effectively suppresses CLP-induced systemic inflammatory responses.

We next measured the serum levels of myocardial injury biomarkers. No significant differences in CK-MB and cTnT levels were observed between the Sham+PBS and Sham+Fer-1 groups. However, the CLP+PBS group had significantly elevated CK-MB and cTnT levels relative to the Sham control, while Fer-1 treatment substantially reduced these cardiac markers in the CLP+Fer-1 group compared to the CLP+PBS group (Fig. 2C,D). Histopathological examination by light microscopy revealed intact myocardial architecture in both the Sham+PBS and Sham+Fer-1 groups. These were characterized by densely and orderly arranged cardiomyocytes with distinct nucleoli, intact nuclear membranes, and the absence of interstitial edema. In contrast, the CLP+PBS group displayed marked pathologi-

cal alterations, including disorganized myocardial cell arrangement, myofibril fragmentation, pronounced cellular and interstitial edema, and obvious inflammatory cell infiltration. Fer-1 treatment significantly ameliorated these histopathological changes in the CLP+Fer-1 group compared to the CLP+PBS controls (Fig. 2E).

Echocardiographic analysis revealed the Sham+Fer-1 group had preserved cardiac function and structure compared to Sham+PBS controls. The CLP+PBS group showed significant reductions in left ventricular end-diastolic volume (LVEDV) and end-systolic volume (LVESV), accompanied by decreased left ventricular internal dimensions, pronounced thickening of ventricular walls and interventricular septum with edema, and indistinct myocardial borders. In contrast, Fer-1 treatment substantially ameliorated these structural alterations in the CLP+Fer-1 group, which showed no statistically significant differences in cardiac parameters compared to the Sham+PBS controls (Fig. 2F–J).

Collectively, these findings demonstrate that pharmacological inhibition of ferroptosis with Fer-1 effectively ameliorated the CLP-induced systemic inflammatory response and mitigated the extent of myocardial injury.

## 3.3 Downregulation of VDAC3 Expression in CLP-induced Myocardial Injury

To further investigate the molecular mechanism underlying ferroptosis regulation in SIMI, transcriptomic and proteomic sequencing were performed on cardiac tissues from the Sham and CLP groups. The integrated analysis identified 35,556 DEGs and 232 DEPs. Compared with the Sham group, the CLP group exhibited 1760 upregulated and 1796 downregulated genes, along with 88 upregulated and 144 downregulated proteins (visualized as heatmaps in Fig. 3A,B). To validate the consistency between transcriptomic and proteomic profiles, intersection analysis was conducted between the downregulated genes and downregulated proteins, as well as between the upregulated genes and upregulated proteins. This analysis revealed 16 commonly downregulated gene/protein pairs and 21 commonly upregulated gene/protein pairs (presented as Venn diagrams in Fig. 3C).

GO enrichment analysis was performed to assess the potential functions of DEPs. The results revealed that DEPs were significantly involved in biological processes including mitochondrial ATP synthesis-coupled electron transport, oxidative phosphorylation, mitochondrial respiratory chain complex assembly, and ATP metabolism. Molecular function analysis suggested regulatory roles for the DEPs in NADH dehydrogenase activity, oxidoreductase activity, and electron transfer activity. Cellular component localization indicated a predominant mitochondrial distribution for the DEPs (Fig. 3D). Separate KEGG pathway analysis of up- and down-regulated DEPs showed significant enrichment in oxidative phosphorylation, HIF-1 signaling



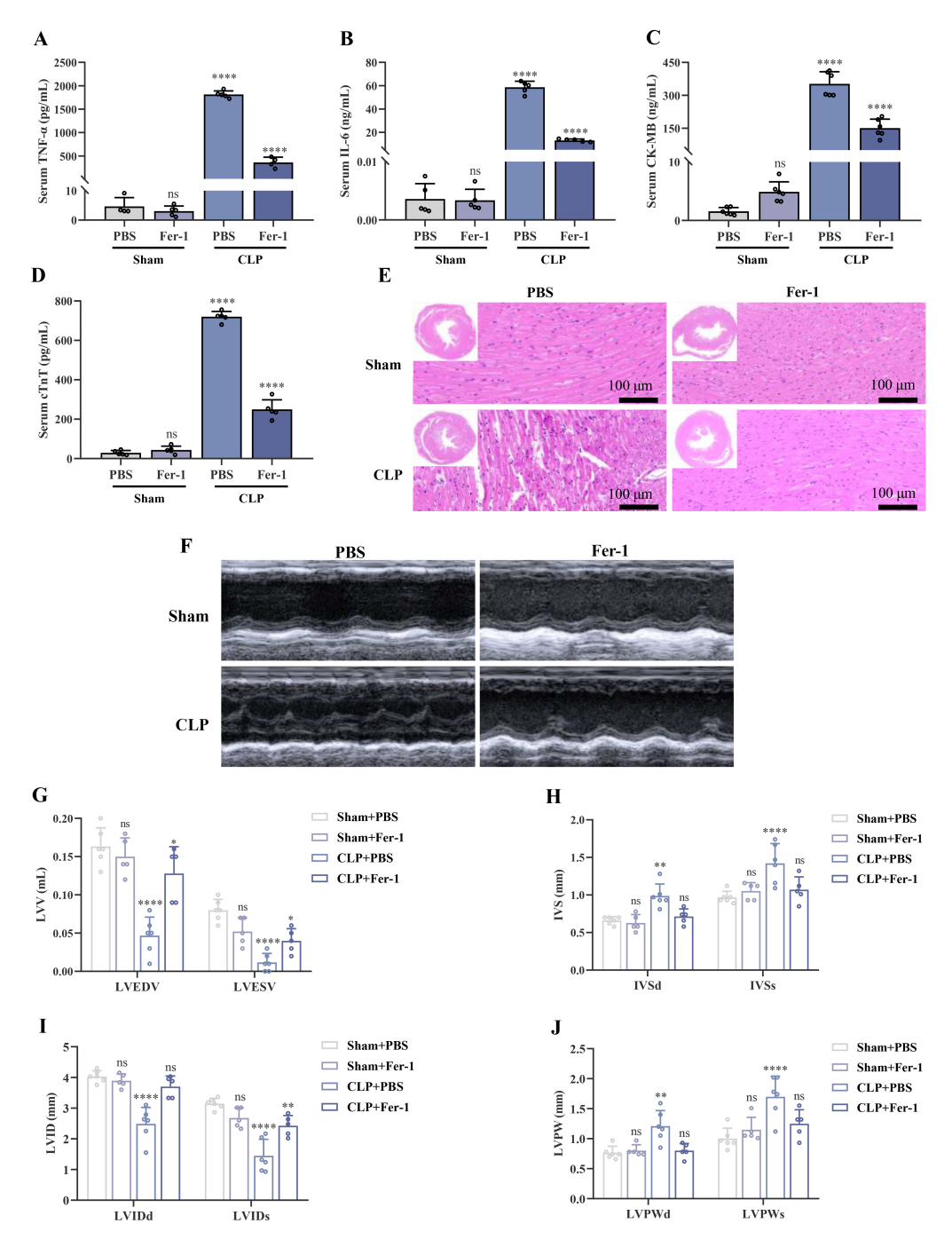


Fig. 2. Inhibition of ferroptosis effectively improved CLP-induced myocardial injury in mice. (A) Serum level of TNF- $\alpha$  (n = 5). (B) Serum level of IL-6 (n = 5). (C) Serum level of CK-MB (n = 6). (D) Serum level of cTnT (n = 5). (E) Representative H&E-stained cardiac section (Scale bar =  $100 \mu m$ , n = 3). (F) Representative echocardiographic images. (G–J) Quantitative analysis of LVV, IVS, LVID, and LVPW (n = 6). Data are presented as the mean  $\pm$  SD. Statistical analysis was performed using one-way ANOVA followed by Tukey's multiple comparisons test. \*p < 0.05, \*\*p < 0.01, \*\*\*\* p < 0.0001, ns p > 0.05. Abbreviations: LVEDV, left ventricular end-diastolic volume; LVESV, left ventricular end-systolic volume; IVSd, interventricular septal end-diastolic thickness; IVIDd, left ventricular end-diastolic internal diameter; LVIDs, left ventricular end-systolic posterior wall thickness; LVPWs, Left ventricular end-systolic posterior wall thickness; TNF- $\alpha$ , tumor necrosis factor- $\alpha$ ; H&E, hematoxylin-eosin; LVV, left ventricular volume; IVS, interventricular septal thickness; LVID, left ventricular internal diameter; LVPW, Left ventricular posterior wall thickness; ANOVA, analysis of variance.

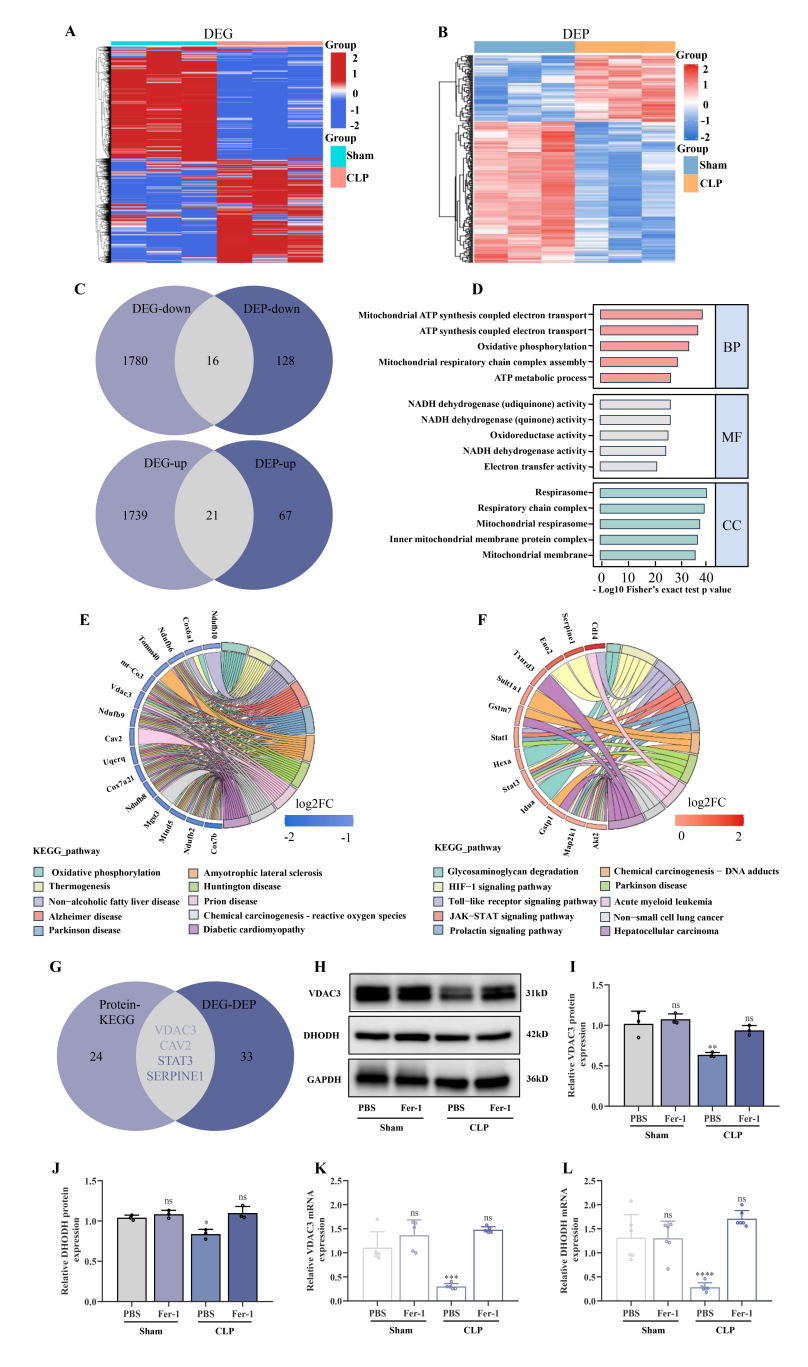


Fig. 3. Downregulation of VDAC3 expression during CLP-induced myocardial injury. (A) Heatmap of DEGs identified from transcriptome analysis of mouse cardiac tissue (n = 3). (B) Heatmap of DEPs identified from transcriptome analysis of mouse cardiac tissue (n = 3). (C) Venn diagrams showing overlap between downregulated DEGs and DEPs, and between upregulated DEGs and DEPs. (D) Bar graph showing results of GO enrichment analysis for identified DEPs: BP, MF, and CC. (E,F) Chord plots of KEGG pathway enrichment analysis for downregulated and upregulated DEPs. (G) Venn diagram showing overlapping proteins between KEGG-enriched DEPs and intersection proteins from Fig. 3C. (H) Representative Western blots showing VDAC3 and DHODH protein expression in mouse cardiac tissue. (I) Quantitative analysis of VDAC3 protein levels in mouse cardiac tissues (n = 3). (J) Quantitative analysis of DHODH protein levels in mouse cardiac tissues (n = 3). (K,L) Quantitative analysis of VDAC3 and DHODH mRNA levels in mouse cardiac tissues (n = 6). Data are presented as the mean  $\pm$  SD. Statistical analysis was performed using one-way ANOVA followed by Tukey's multiple comparisons test. \* p < 0.05, \*\*p < 0.01, \*\*\*\*p < 0.001, \*\*\*\*p < 0.0001, ns p > 0.05. Abbreviations: DEGs, differentially expressed genes; DEPs, differentially expressed proteins; GO, gene ontology; BP, biological process; MF, molecular function; CC, cellular component; VDAC3, voltage-dependent anion channel 3; CLP, cecal ligation and puncture; KEGG, Kyoto Encyclopedia of Genes and Genomes; DHODH, dihydroorotate dehydrogenase.

pathway, Toll-like receptor signaling pathway, JAK-STAT signaling pathway, and various disease-related pathways. Variations in the expression of significantly enriched proteins across distinct biological pathways were visually represented through chord diagrams (Fig. 3E,F).

To identify key DEPs, we performed intersection analysis between 28 KEGG-enriched DEPs and 37 DEGs/DEPs with overlapping transcriptomic and proteomic profiles. This consistently yielded four DEGs/DEPs (Fig. 3G). VDAC3 is an abundant protein in the OMM that regulates metabolite transport between the mitochondria and cytoplasm [22], as well as the protection of mitochondria from oxidative stress-induced damage [40]. Since both KEGG and GO enrichment analyses suggested that cardiac tissue injury in the CLP group was associated with oxidative phosphorylation and mitochondrial dysfunction, VDAC3 was selected as the key DEG/DEP for further investigation. The DHODH enzyme localizes to the outer surface of the IMM and is a recently identified non-canonical ferroptosis defense pathway, independent of the classical GPX4 axis [31]. The inactivation of mitochondrial DHODH triggers extensive lipid peroxidation within mitochondria and induces ferroptosis [41].

We next conducted Western blotting and qRT-PCR analyses of murine cardiac tissues to study potential changes in the protein and mRNA expression of VDAC3 and DHODH during SIMI. Comparative analysis revealed no significant differences in VDAC3 and DHODH expression at both the protein and mRNA levels between the Sham+PBS and Sham+Fer-1 groups. However, the expression of both VDAC3 and DHODH was markedly lower in the CLP+PBS group compared to the Sham controls. Fer-1 treatment in the CLP+Fer-1 group significantly attenuated these decreases, resulting in elevated expression relative to the CLP+PBS group (Fig. 3H–L).

These findings suggest that VDAC3 potentially modulates mitochondrial homeostasis to regulate ferroptosis and exert cardioprotective effects in SIMI through the DHODH pathway.

### 3.4 Decreased VDAC3 Levels in the Serum of Septic Patients

Serum samples were collected from healthy controls and from septic patients for assessment of the VDAC3 level using ELISA. Correlation analyses were subsequently performed between the VDAC3 level and various clinical indices in the sepsis group, including white blood cells (WBC), lactate dehydrogenase (LDH), neutrophil percentage (N%), C-reactive protein (CRP), and platelets (PLT). VDAC3 levels were found to be significantly lower in sepsis patients compared to healthy controls (Fig. 4A). Furthermore, the serum level of VDAC3 was negatively correlated with the level of WBC (r = -0.4670, p = 0.0106) and the N% (r = -0.4350, p = 0.0184) (Fig. 4B,C), and positively correlated with the levels of LDH (r = 0.5335, p = 0.0029)

and PLT (r = 0.4603, p = 0.0120) (Fig. 4D,E). Moreover, the VDAC3 level showed no significant correlation with CRP (r = -0.1520, p = 0.4312) (Fig. 4F).

These results are consistent with our *in vivo* experimental findings, and implicate VDAC3 in sepsis-related inflammatory responses and organ damage.

#### 3.5 LPS Induced Ferroptosis in HL-1 Cardiomyocytes

LPS is the major pathogenic component of Gramnegative bacteria. It was used here to establish an experimental, *in vitro* inflammatory injury model using HL-1 cardiomyocytes. HL-1 cardiomyocytes were first treated with 1 µg/mL LPS, followed by measurement of TNF- $\alpha$  levels in the cell supernatant using ELISA. Significant elevation of the TNF- $\alpha$  concentration was found in the LPS group compared with the Con group (Fig. 5A). Furthermore, quantitative analysis revealed markedly upregulated expression of IL-6 and IL-1 $\beta$  mRNA in LPS-stimulated cardiomyocytes (Fig. 5B,C). Collectively, these findings confirm successful establishment of the LPS-induced inflammatory injury model in HL-1 cardiomyocytes.

Given that lipid peroxidation is a critical hallmark of ferroptosis, we next measured the levels of the lipid peroxidation product MDA and of glutathione in cardiomyocytes. Compared with the Con group, LPS-treated cardiomyocytes showed significant reductions in total glutathione content, GSH, and the GSH/GSSG ratio (Fig. 5E–G), along with a markedly increased MDA level (Fig. 5D). Furthermore, flow cytometric analysis revealed increased lipid peroxidation in LPS-stimulated HL-1 cardiomyocytes compared to the Con group (Fig. 5H,I). Together, these findings indicate that LPS stimulation of cardiomyocytes induces an imbalance in the mitochondrial antioxidant system.

Subsequently, we evaluated the expression of ferroptosis-related proteins in HL-1 cardiomyocytes. Compared with the Con group, the LPS group showed significantly reduced expression of GPX4 and SLC7A11 protein (Fig. 5J–L), and markedly increased expression of ferritin protein (Fig. 5J,M). Moreover, qRT-PCR analysis revealed that LPS treatment significantly decreased the expression of GPX4 and SLC7A11 mRNA in HL-1 cardiomyocytes (Fig. 5N,O), but substantially increased the expression of PTGS2 mRNA (Fig. 5P) compared to the control group. Collectively, these findings indicate that LPS induces ferroptosis in HL-1 cardiomyocytes.

We also performed Western blot and qRT-PCR analyses to evaluate the expression of VDAC3 and DHODH in HL-1 cardiomyocytes at the protein and mRNA levels. The LPS group showed significantly reduced protein and mRNA expression of both VDAC3 and DHODH compared with the Con group (Fig. 5Q–U). These findings suggest that VDAC3 and DHODH play crucial roles in LPS-induced myocardial injury.



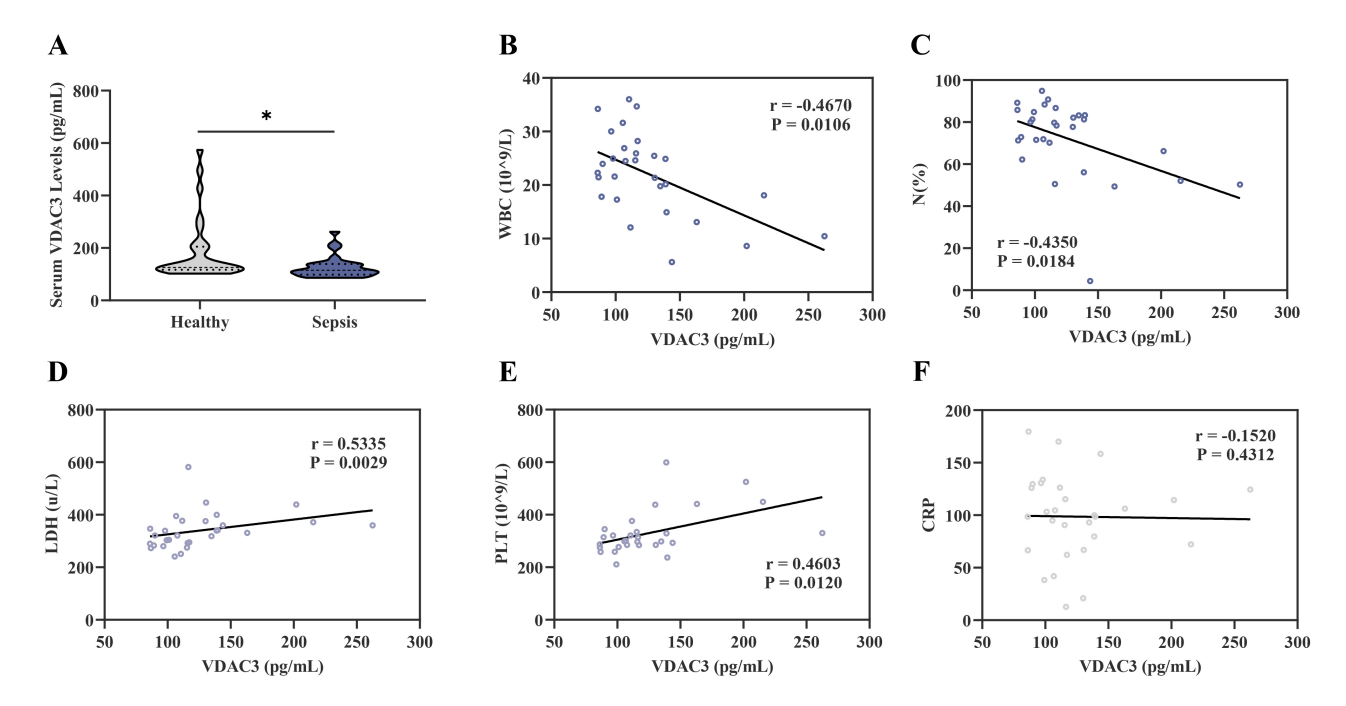


Fig. 4. Decreased VDAC3 level in the serum of septic patients. (A) Serum VDAC3 levels in healthy controls and in septic children (n = 29). (B) Negative correlation between VDAC3 level and WBC in septic children (n = 29). (C) Negative correlation between VDAC3 level and N% in septic children (n = 29). (D) Positive correlation between VDAC3 level and LDH in septic children (n = 29). (E) Positive correlation between VDAC3 level and PLT in septic children (n = 29). (F) No significant correlation was found between the VDAC3 level and CRP in septic children (n = 29). Data are presented as the mean  $\pm$  SD. Statistical significance was determined with the unpaired two-tailed Student's *t*-test. Spearman correlation analysis was employed to evaluate associations between continuous variables. \* p < 0.05, Abbreviations: WBC, white blood cells; LDH, lactate dehydrogenase; N%, neutrophil percentage; CRP, C-reactive protein; PLT, platelets.

#### 3.6 Overexpression of VDAC3 Regulates Ferroptosis

To further investigate the mechanism involving VDAC3 in SIMI, a VDAC3-overexpression plasmid was transfected into HL-1 cardiomyocytes. Fluorescence microscopy revealed the transfection efficiency was >80% (Fig. 6A), indicating optimal transfection conditions for subsequent functional studies. The CCK-8 cell proliferation assay demonstrated significantly increased cell proliferation in the VDAC3 overexpression (OE) group compared to the negative control (NC) group at 24 h, 48 h, and 72 h post-transfection (Fig. 6B). This result indicates that VDAC3 overexpression promotes the proliferation of HL-1 cardiomyocytes.

We also evaluated the effects of VDAC3 overexpression in HL-1 cardiomyocytes on the expression of ferroptosis-related genes at the protein and mRNA level. Western blot analysis revealed that VDAC3 overexpression significantly increased the protein expression of DHODH and GPX4, while markedly downregulating the expression of ferritin (Fig. 6C–G). These findings indicate that VDAC3 overexpression modulates the expression of ferroptosis-associated proteins in HL-1 cardiomyocytes. Furthermore, the results of qRT-PCR showed that VDAC3 overexpression substantially increased the mRNA levels of DHODH,

SLC7A11 and GPX4, but significantly reduced those of PTGS2 and ACSL4 (Fig. 6H–M). Hence, VDAC3 overexpression appears to regulate the transcriptional expression of ferroptosis-related genes in HL-1 cardiomyocytes.

Excessive intracellular ROS production accompanied by depletion of the antioxidant GSH both contribute to oxidative stress. We next used the DCFH-DA fluorescent probe to evaluate the effects of VDAC3 overexpression on ROS levels in HL-1 cardiomyocytes. The OE and NC groups showed no significant difference in ROS level. However, the LPS-treated NC group (NC-LPS) exhibited markedly elevated ROS production, while VDAC3-overexpressing LPS-treated cells (OE-LPS) showed significantly reduced ROS levels compared to the NC-LPS group (Fig. 6N,O). These results indicate that VDAC3 overexpression can significantly reduce LPS-induced ROS generation.

Lipid peroxidation leads to structural and functional alterations of critical membrane proteins, ultimately leading to cellular dysfunction and extensive tissue damage. Flow cytometric analysis using the BODIPY 581/591 C11 fluorescent probe revealed no significant difference in lipid peroxidation between the OE and NC groups under basal conditions. Stimulation with LPS significantly increased



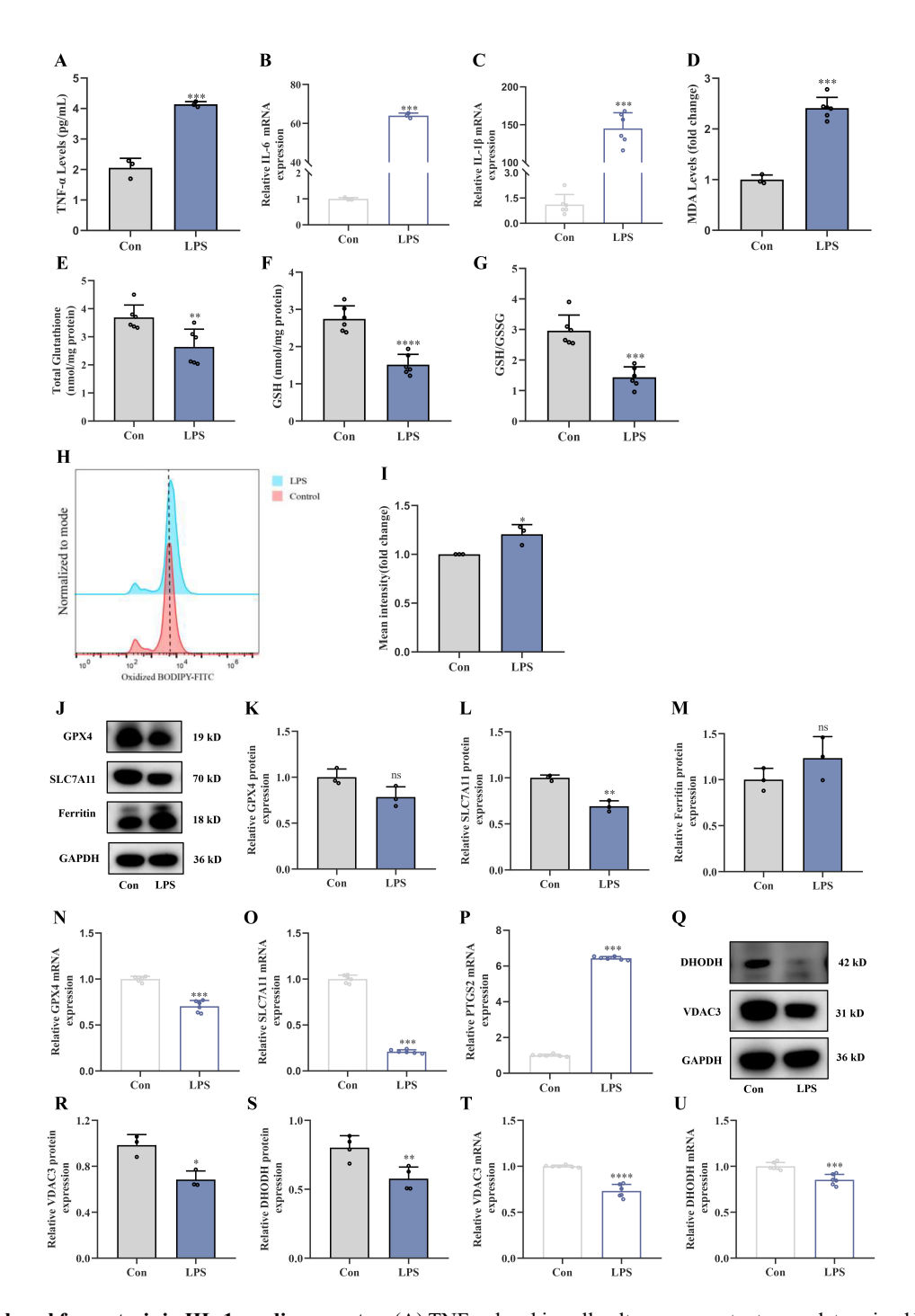


**Fig. 5.** LPS induced ferroptosis in HL-1 cardiomyocytes. (A) TNF- $\alpha$  level in cell culture supernatants was determined by ELISA (n = 3). (B) Quantitative analysis of IL-6 mRNA expression in cardiomyocytes (n = 3). (C) Quantitative analysis of IL-1 $\beta$  mRNA expression in cardiomyocytes (n = 6). (D) MDA content was measured using colorimetric assay (n = 6). (E) Total glutathione level (n = 6). (F) GSH concentration (n = 6). (G) GSH/GSSG ratio in cellular extracts (n = 6). (H,I) Quantitative assessment of lipid peroxidation by flow cytometry (n = 3). (J–M) Western blotting analysis of GPX4, SLC7A11 and ferritin protein expression (n = 3). (N–P) GPX4, SLC7A11, and PTGS2 mRNA levels were quantified by qRT-PCR (n = 6). (Q–S) Protein expression of DHODH and VDAC3 was evaluated by Western blotting (n = 3). (T,U) Relative mRNA expression levels of DHODH and VDAC3 were determined by qRT-PCR (n = 6). Data are presented as the mean ± SD. Statistical significance was determined using unpaired two-tailed Student's *t*-tests. \* p < 0.05, \*\* p < 0.01, \*\*\*\* p < 0.001, \*\*\*\* p < 0.0001, ns p > 0.05. Abbreviations: Con, control; LPS, lipopolysaccharide; MDA, Malondialdehyde; GSH, reduced glutathione; GSSG, oxidized glutathione; HL-1, a murine cardiomyocyte cell line; ELISA, enzyme-linked immunosorbent assay; IL, interleukin.



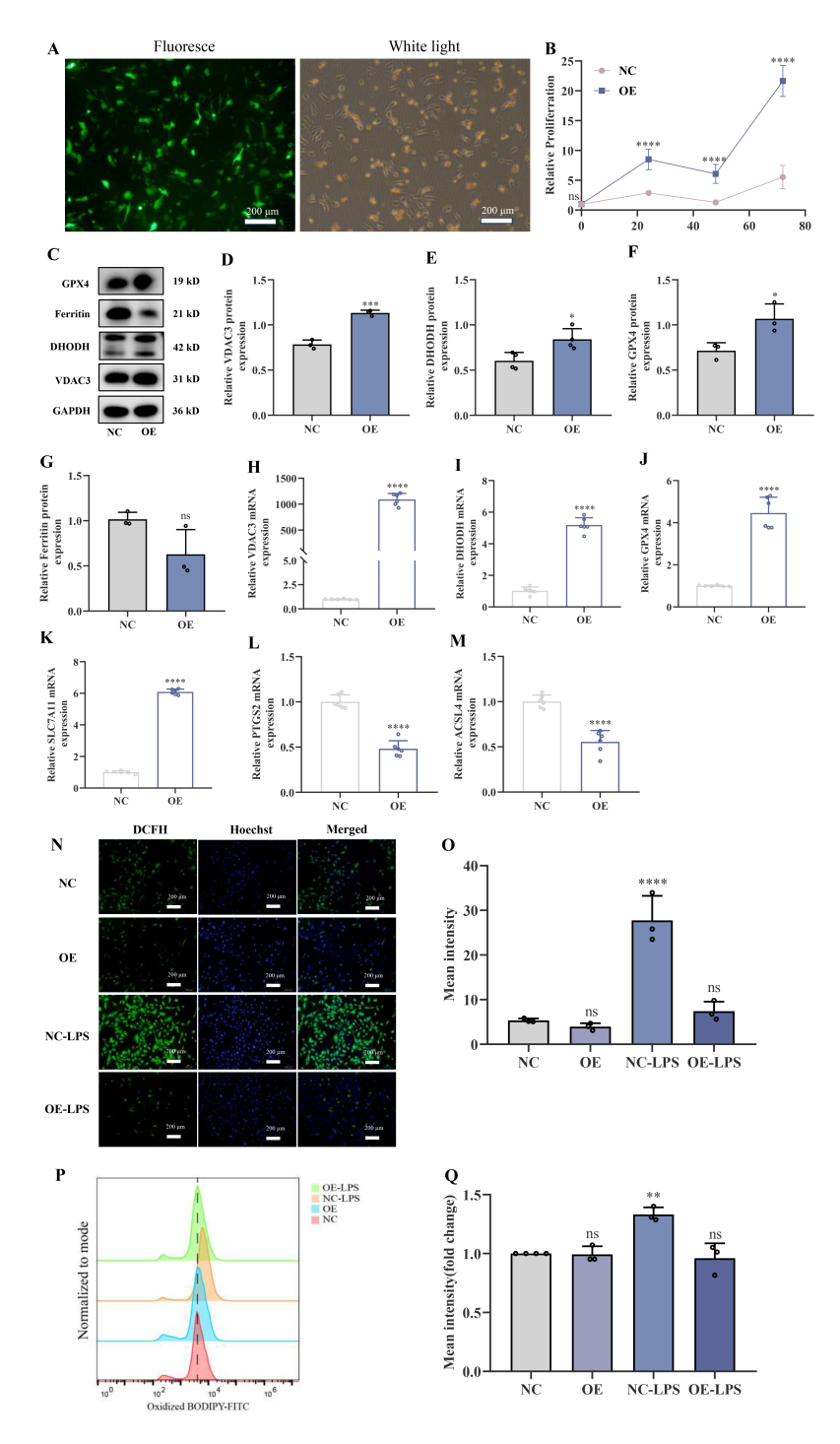


Fig. 6. Overexpression of VDAC3 regulates ferroptosis. (A) The transfection efficiency of VDAC3-overexpressing plasmids in HL1 cardiomyocytes was demonstrated by fluorescence microscopy (Scale bar = 200  $\mu$ m). (B) Cell proliferation was assessed using the CCK-8 assay (n = 6). (C) Protein expression levels of GPX4, ferritin, DHODH, and VDAC3 were evaluated by Western blotting and subsequently quantified. (D) VDAC3 protein expression (n = 3). (E) DHODH protein expression (n = 4). (F) GPX4 protein expression (n = 3). (G) Ferritin protein expression (n = 3). (H–M) Relative mRNA expression levels of VDAC3, DHODH, GPX4, SLC7A11, PTGS2, and ACSL4 were quantified by qRT-PCR (n = 6). (N,O) Intracellular ROS levels were measured by fluorescence microscopy (Scale bar = 200  $\mu$ m; n = 3). (P,Q) Intracellular lipid peroxidation was evaluated by flow cytometry (n = 3). Data are presented as the mean  $\pm$  SD. Statistical analyses were performed using two-way ANOVA with Sidak's multiple comparisons test (B), one-way ANOVA with Tukey's multiple comparisons test (N–Q), or multiple unpaired two-tailed Student's *t*-tests (C–M). \* p < 0.05, \*\* p < 0.01, \*\*\*\* p < 0.001, \*\*\*\* p < 0.001, \*\*\*\* p < 0.001, \*\*\*\*\* p < 0.001, \*\*\*\* p < 0.001, \*\*\*\* p < 0.001, \*\*\*\* p < 0.001, \*\*\*\*

lipid peroxidation in the NC-LPS group compared to untreated controls, whereas the OE-LPS group showed substantially decreased lipid peroxidation relative to the NC-LPS group (Fig. 6P,Q). This indicates that VDAC3 overexpression effectively mitigates LPS-induced lipid peroxidation in HL-1 cardiomyocytes.

#### 4. Discussion

The results of this study found that ferroptosis plays a critical role in CLP-induced myocardial injury, and that inhibition of ferroptosis significantly ameliorates cardiac damage in mice. Furthermore, *in vivo* and *in vitro* models revealed significant downregulation of VDAC3 and DHODH expression, while inhibition of ferroptosis markedly upregulated their expression in cardiac tissues. Importantly, the serum level of VDAC3 was significantly lower in pediatric sepsis patients and correlated with certain clinical indicators of sepsis. Additionally, VDAC3 overexpression effectively upregulated the expression of DHODH, reduced mitochondrial oxidative stress, and regulated LPS-induced ferroptosis.

SIMI is the predominant manifestation of septic cardiac dysfunction, with an incidence of up to 50% [42]. The pathophysiological processes of SIMI include impaired ATP production, dysregulated Ca<sup>2+</sup> homeostasis, mitochondrial permeability transition pore dysfunction, and excessive generation of oxygen-free radicals [43]. The mechanisms underlying SIMI are complex and remain to be fully elucidated. However, current evidence indicates the lipolysis rate is significantly increased during the acute phase of sepsis through a process regulated by pro-inflammatory cytokines, stress hormones and insulin [44]. Oxidative stress and inflammation play a critical role in sepsis-induced cardiac injury [45]. Myocardial protection during sepsis may be achieved with therapeutic interventions that attenuate iron overload, reduce oxidative stress, and modulate the inflammatory response [46]. Additionally, the accumulation of lipid droplets in damaged cardiomyocytes suggests that impaired transport of fatty acids into mitochondria may be a potential mechanism that contributes to SIMI [47].

Ferroptosis is a regulated cell death pathway characterized by iron-dependent accumulation of lipid peroxides [48,49], with multiple studies implicating this pathway in SIMI [36,50]. The first-generation ferroptosis inhibitor Fer-1 has been employed extensively in the investigation of various diseases, including cardiovascular disorders [51]. In our experimental design, intraperitoneal administration of Fer-1 at 2 h after CLP modeling effectively suppressed CLP-induced ferroptosis and ameliorated myocardial injury. We also established an LPS-induced HL-1 cardiomyocyte model of myocardial injury. Evaluation of classic ferroptosis markers in this model confirmed the association between ferroptosis and LPS-mediated cardiomyocyte damage. Given the complex regulatory role of mitochondria in ferroptosis, additional studies are required to

elucidate the underlying mechanisms by which mitochondrial homeostasis is maintained under septic stress.

Mitochondria play a pivotal role in orchestrating fundamental metabolic processes, redox homeostasis, and calcium regulation, with substantial evidence supporting a direct association between mitochondrial dysfunction and ferroptosis [52]. These essential organelles are critical for maintaining cellular functionality in cardiomyocytes, and their impairment leads to myocardial cell dysfunction [53– 55]. Mitochondrial membrane phospholipids are essential for maintaining structural integrity, respiratory protein activity, and protein trafficking to mitochondria. The double-membrane architecture of mitochondria consists of an OMM and an IMM, with the latter serving as the principal site for electron transport chain activity and ATP generation [56]. These membranes contain numerous specialized proteins that regulate diverse cellular functions between the endoplasmic reticulum and mitochondria, including lipid metabolism, calcium signaling, inflammatory responses, and programmed cell death pathways [57].

Emerging evidence suggests that VDAC3 may participate in ferroptosis through molecular mechanisms that involve modulation of the mitochondrial membrane potential and redox homeostasis [28–30]. However, the precise role of VDAC3 remains controversial. Notably, the canonical ferroptosis inducer Erastin has been demonstrated to bind directly to VDAC2/3 isoforms. This impairs the electron transfer efficiency of NADH dehydrogenase complexes by altering OMM permeability, ultimately triggering cellular ferroptosis [58,59]. Although both VDAC2 and VDAC3 can serve as direct molecular targets of Erastin, current research has led to a relatively thorough understanding of the VDAC2 regulatory network. This encompasses its functional characteristics in the transport of mitochondrial metabolites, maintenance of calcium homeostasis, and suppression of apoptosis [23,60,61]. In contrast, the molecular mechanisms underlying the involvement of VDAC3 in ferroptosis remain enigmatic. Critical questions remain regarding its potential involvement in distinct signaling transduction pathways for cell death, as well as its interaction networks with other ferroptosis-associated proteins [62,63].

DHODH is localized to the IMM and participates in the *de novo* pyrimidine nucleotide synthesis pathway, which represents a recently identified mitochondrial defense mechanism against ferroptosis [32,36]. We hypothesize that activation of ferroptosis during septic myocardial injury may be closely associated with mitochondrial dysfunction. A previous study has demonstrated a critical role for VDAC in cellular apoptosis [64]. Although VDAC3 has been shown to protect mitochondria from oxidative stress-induced damage, the underlying molecular mechanisms remain unclear [40]. Using mass spectrometry analysis, Yang *et al.* [65] showed that VDAC3 interacts with DHODH, thereby bridging the pyrimidine biosynthesis complex to IMM-anchored DHODH to form a multi-enzyme complex



termed the "pyrimidinosome". This process is regulated by AMP-activated protein kinase (AMPK), which dissociates from the complex to enhance pyrimidinosome assembly and inactivate uridine 5′-monophosphate synthase, thereby promoting DHODH-mediated defense against ferroptosis [65].

We observed significant downregulation of VDAC3 and DHODH in both CLP-induced cardiac tissues and in LPS-stimulated cardiomyocytes. Notably, treatment with the ferroptosis inhibitor Fer-1 substantially upregulated both VDAC3 and DHODH mRNA and protein expression in murine cardiac tissues, suggesting their involvement in ferroptosis regulation. Furthermore, marked downregulation of VDAC3 was observed in serum samples from septic patients, and significant correlations were observed between VDAC3 and the clinical parameters of WBC, N%, LDH, and PLT. In addition, our findings demonstrated that overexpression of VDAC3 alleviated LPS-induced mitochondrial oxidative stress and lipid peroxidation, indicating the critical role of VDAC3 in ferroptosis.

N-carbamoyl-L-aspartate is an intermediate in the *de novo* pyrimidine biosynthesis pathway upstream of DHODH. This molecule was significantly depleted following treatment of cancer cells with a GPX4 inhibitor. In contrast, the downstream DHODH metabolite uridine accumulated after treatment, indicating complementary roles for GPX4 and DHODH in the suppression of ferroptosis [66]. In summary, the current results showed that VDAC3 overexpression upregulated the expression of DHODH and modulated ferroptosis signaling pathways, indicating a potential regulatory mechanism in which VDAC3 governs ferroptosis through DHODH-mediated pathways. However, the upstream signaling molecules that regulate VDAC3 remain unknown and warrant further investigation.

#### 5. Conclusions

In summary, this study suggests that ferroptosis is a significant contributor to SIMI, and that administration of Fer-1 effectively mitigates cardiac damage by inhibiting ferroptosis. Furthermore, the VDAC3/DHODH signaling axis was found to maintain mitochondrial homeostasis, thereby regulating ferroptosis and conferring myocardial protection. These findings suggest that therapeutic targeting of the VDAC3/DHODH regulatory mechanism may be a promising intervention strategy for SIMI.

#### Availability of Data and Materials

All data supporting the findings of this study will be shared by the corresponding author ZHT and HJ upon reasonable request.

#### **Author Contributions**

JH, HTZ, JLW, and FZ designed the research study. JLW, FZ, and CQT performed the research. NNW, HZ,

YY, YC, and XH contributed to the design of the methodology and conducted the formal data analysis. XXX, ZJB, LS, and QQX made substantial contributions to the investigation of the study. JLW analyzed the data. JH, HTZ, JLW, and FZ wrote the manuscript. JH provided help for funding acquisition. All authors contributed to editorial changes in the manuscript. All authors read and approved the final manuscript. All authors have participated sufficiently in the work and agreed to be accountable for all aspects of the work.

#### **Ethics Approval and Consent to Participate**

The study was carried out in accordance with the guidelines of the Declaration of Helsinki. The study protocol was reviewed and approved by the Medical Ethics Committee of the Children's Hospital of Soochow University (2024CS169), and written informed consent was obtained from the guardians of all participants. All animal experiments were conducted in accordance with the requirements of the Animal Experimentation and Ethics Committee of Soochow University (SUDA20241104A02), adhering to the *3R* principles throughout the experimental process.

#### Acknowledgment

We gratefully acknowledge the assistance of nurses from the Department of Cardiology and investigators from the Institute of Pediatric Research at the Children's Hospital of Soochow University.

#### **Funding**

This research was funded by the National Natural Science Foundation of China (82472207); Jiangsu Provincial Science and Technology Project (BE2023714); and Suzhou Science and Technology Development Project (SKY2023058 and SKJY2021108).

#### **Conflict of Interest**

The authors declare no conflict of interest.

#### References

- Singer M, Deutschman CS, Seymour CW, Shankar-Hari M, Annane D, Bauer M, et al. The Third International Consensus Definitions for Sepsis and Septic Shock (Sepsis-3). JAMA. 2016; 315: 801–810. https://doi.org/10.1001/jama.2016.0287.
- [2] Jacobi J. The pathophysiology of sepsis-2021 update: Part 1, immunology and coagulopathy leading to endothelial injury. American Journal of Health-system Pharmacy: AJHP: Official Journal of the American Society of Health-System Pharmacists. 2022; 79: 329–337. https://doi.org/10.1093/ajhp/zxab380.
- [3] Hong G, Zheng D, Zhang L, Ni R, Wang G, Fan GC, et al. Administration of nicotinamide riboside prevents oxidative stress and organ injury in sepsis. Free Radical Biology & Medicine. 2018; 123: 125–137. https://doi.org/10.1016/j.freeradbiomed. 2018.05.073.
- [4] Shankar-Hari M, Phillips GS, Levy ML, Seymour CW, Liu VX, Deutschman CS, et al. Developing a New Definition and



- Assessing New Clinical Criteria for Septic Shock: For the Third International Consensus Definitions for Sepsis and Septic Shock (Sepsis-3). JAMA. 2016; 315: 775–787. https://doi.org/10.1001/jama.2016.0289.
- [5] Carbone F, Liberale L, Preda A, Schindler TH, Montecucco F. Septic Cardiomyopathy: From Pathophysiology to the Clinical Setting. Cells. 2022; 11: 2833. https://doi.org/10.3390/cells11182833.
- [6] Vieillard-Baron A, Caille V, Charron C, Belliard G, Page B, Jardin F. Actual incidence of global left ventricular hypokinesia in adult septic shock. Critical Care Medicine. 2008; 36: 1701– 1706. https://doi.org/10.1097/CCM.0b013e318174db05.
- [7] Dong Y, Wei S, Liu Y, Ji X, Yin X, Wu Z, et al. Aspirin is associated with improved outcomes in patients with sepsis-induced myocardial injury: An analysis of the MIMIC-IV database. Journal of Clinical Anesthesia. 2024; 99: 111597. https://doi.org/10.1016/j.jclinane.2024.111597.
- [8] Liu C, Zou Q, Tang H, Liu J, Zhang S, Fan C, et al. Melanin nanoparticles alleviate sepsis-induced myocardial injury by suppressing ferroptosis and inflammation. Bioactive Materials. 2022; 24: 313–321. https://doi.org/10.1016/j.bioactmat.2022. 12.026.
- [9] Huang J, Ita M, Zhou H, Zhao H, Hassan F, Bai Z, et al. Autophagy induced by taurolidine protects against polymicrobial sepsis by promoting both host resistance and disease tolerance. Proceedings of the National Academy of Sciences of the United States of America. 2022; 119: e2121244119. https://doi.org/10.1073/pnas.2121244119.
- [10] Kuroshima T, Kawaguchi S, Okada M. Current Perspectives of Mitochondria in Sepsis-Induced Cardiomyopathy. International Journal of Molecular Sciences. 2024; 25: 4710. https://doi.org/ 10.3390/ijms25094710.
- [11] Lopaschuk GD, Karwi QG, Tian R, Wende AR, Abel ED. Cardiac Energy Metabolism in Heart Failure. Circulation Research. 2021; 128: 1487–1513. https://doi.org/10.1161/CIRCRESAHA. 121.318241.
- [12] Dixon SJ, Lemberg KM, Lamprecht MR, Skouta R, Zaitsev EM, Gleason CE, *et al.* Ferroptosis: an iron-dependent form of nonapoptotic cell death. Cell. 2012; 149: 1060–1072. https://doi.org/10.1016/j.cell.2012.03.042.
- [13] Dai E, Chen X, Linkermann A, Jiang X, Kang R, Kagan VE, et al. A guideline on the molecular ecosystem regulating ferroptosis. Nature Cell Biology. 2024; 26: 1447–1457. https://doi.org/10.1038/s41556-024-01360-8.
- [14] Gao W, Wang X, Zhou Y, Wang X, Yu Y. Autophagy, ferroptosis, pyroptosis, and necroptosis in tumor immunotherapy. Signal Transduction and Targeted Therapy. 2022; 7: 196. https://doi.org/10.1038/s41392-022-01046-3.
- [15] Stockwell BR, Jiang X, Gu W. Emerging Mechanisms and Disease Relevance of Ferroptosis. Trends in Cell Biology. 2020; 30: 478–490. https://doi.org/10.1016/j.tcb.2020.02.009.
- [16] Wu D, Spencer CB, Ortoga L, Zhang H, Miao C. Histone lactylation-regulated METTL3 promotes ferroptosis via m6Amodification on ACSL4 in sepsis-associated lung injury. Redox Biology. 2024; 74: 103194.
- [17] Shen H, Xie K, Tian Y, Wang X. N6-methyladenosine writer METTL3 accelerates the sepsis-induced myocardial injury by regulating m6A-dependent ferroptosis. Apoptosis: an International Journal on Programmed Cell Death. 2023; 28: 514–524. https://doi.org/10.1007/s10495-022-01808-y.
- [18] Wen Q, Liu J, Kang R, Zhou B, Tang D. The release and activity of HMGB1 in ferroptosis. Biochemical and Biophysical Research Communications. 2019; 510: 278–283. https://doi.org/10.1016/j.bbrc.2019.01.090.
- [19] Fang X, Ardehali H, Min J, Wang F. The molecular and metabolic landscape of iron and ferroptosis in cardiovascular

- disease. Nature Reviews. Cardiology. 2023; 20: 7–23. https://doi.org/10.1038/s41569-022-00735-4.
- [20] Stockwell BR. Ferroptosis turns 10: Emerging mechanisms, physiological functions, and therapeutic applications. Cell. 2022; 185: 2401–2421. https://doi.org/10.1016/j.cell.2022.06. 003
- [21] Zhang Z, Zhou H, Gu W, Wei Y, Mou S, Wang Y, et al. CGI1746 targets σ<sub>1</sub>R to modulate ferroptosis through mitochondria-associated membranes. Nature Chemical Biology. 2024; 20: 699–709. https://doi.org/10.1038/s41589-023-01512-1.
- [22] Kanwar P, Sanyal SK, Mahiwal S, Ravi B, Kaur K, Fernandes JL, et al. CIPK9 targets VDAC3 and modulates oxidative stress responses in Arabidopsis. The Plant Journal: for Cell and Molecular Biology. 2022; 109: 241–260. https://doi.org/10.1111/tpj. 15572.
- [23] Yuan Z, Dewson G, Czabotar PE, Birkinshaw RW. VDAC2 and the BCL-2 family of proteins. Biochemical Society Transactions. 2021; 49: 2787–2795. https://doi.org/10.1042/BS T20210753.
- [24] Okazaki M, Kurabayashi K, Asanuma M, Saito Y, Dodo K, Sodeoka M. VDAC3 gating is activated by suppression of disulfide-bond formation between the N-terminal region and the bottom of the pore. Biochimica et Biophysica Acta. 2015; 1848: 3188–3196. https://doi.org/10.1016/j.bbamem.2015.09.017.
- [25] Zinghirino F, Pappalardo XG, Messina A, Nicosia G, De Pinto V, Guarino F. VDAC Genes Expression and Regulation in Mammals. Frontiers in Physiology. 2021; 12: 708695. https://doi.org/10.3389/fphys.2021.708695.
- [26] Reina S, Checchetto V, Saletti R, Gupta A, Chaturvedi D, Guardiani C, et al. VDAC3 as a sensor of oxidative state of the intermembrane space of mitochondria: the putative role of cysteine residue modifications. Oncotarget. 2016; 7: 2249–2268. https://doi.org/10.18632/oncotarget.6850.
- [27] Geisler S, Holmström KM, Treis A, Skujat D, Weber SS, Fiesel FC, et al. The PINK1/Parkin-mediated mitophagy is compromised by PD-associated mutations. Autophagy. 2010; 6: 871–878. https://doi.org/10.4161/auto.6.7.13286.
- [28] Huang G, Xiang Z, Wu H, He Q, Dou R, Lin Z, et al. The lncRNA BDNF-AS/WDR5/FBXW7 axis mediates ferroptosis in gastric cancer peritoneal metastasis by regulating VDAC3 ubiquitination. International Journal of Biological Sciences. 2022; 18: 1415–1433. https://doi.org/10.7150/ijbs.69454.
- [29] Yang Y, Luo M, Zhang K, Zhang J, Gao T, Connell DO, et al. Nedd4 ubiquitylates VDAC2/3 to suppress erastin-induced ferroptosis in melanoma. Nature Communications. 2020; 11: 433. https://doi.org/10.1038/s41467-020-14324-x.
- [30] Huang F, Pang J, Xu L, Niu W, Zhang Y, Li S, et al. Hedyotis diffusa injection induces ferroptosis via the Bax/Bcl2/VDAC2/3 axis in lung adenocarcinoma. Phytomedicine: International Journal of Phytotherapy and Phytopharmacology. 2022; 104: 154319. https://doi.org/10.1016/j.phymed.2022.154319.
- [31] Mao C, Liu X, Zhang Y, Lei G, Yan Y, Lee H, et al. DHODH-mediated ferroptosis defence is a targetable vulnerability in cancer. Nature. 2021; 593: 586–590. https://doi.org/10.1038/s41586-021-03539-7.
- [32] Löffler M, Jöckel J, Schuster G, Becker C. Dihydroorotatubiquinone oxidoreductase links mitochondria in the biosynthesis of pyrimidine nucleotides. Molecular and Cellular Biochemistry. 1997; 174: 125–129.
- [33] Peters GJ. Re-evaluation of Brequinar sodium, a dihydroorotate dehydrogenase inhibitor. Nucleosides, Nucleotides & Nucleic Acids. 2018; 37: 666–678. https://doi.org/10.1080/15257770. 2018.1508692.
- [34] Tian Y, Xie Y, Guo Z, Feng P, You Y, Yu Q. 17β-oestradiol inhibits ferroptosis in the hippocampus by upregulating DHODH and further improves memory decline after ovariectomy. Re-



- dox Biology. 2023; 62: 102708. https://doi.org/10.1016/j.redox.2023.102708.
- [35] Guerrero-Hue M, García-Caballero C, Palomino-Antolín A, Rubio-Navarro A, Vázquez-Carballo C, Herencia C, et al. Curcumin reduces renal damage associated with rhabdomyolysis by decreasing ferroptosis-mediated cell death. FASEB Journal: Official Publication of the Federation of American Societies for Experimental Biology. 2019; 33: 8961–8975. https://doi.org/10. 1096/fj.201900077R.
- [36] Van Coillie S, Van San E, Goetschalckx I, Wiernicki B, Mukhopadhyay B, Tonnus W, et al. Targeting ferroptosis protects against experimental (multi)organ dysfunction and death. Nature Communications. 2022; 13: 1046. https://doi.org/10.1038/s41467-022-28718-6.
- [37] Samokhvalov V, Jamieson KL, Vriend J, Quan S, Seubert JM. CYP-epoxygenase metabolites of docosahexaenoic acid protect HL-1 cardiac cells against LPS-induced cytotoxicity Through SIRT1. Cell Death Discovery. 2015; 1: 10.1038/cddiscovery.2015.54. https://doi.org/10.1038/cddiscovery.2015.54.
- [38] Ma XH, Liu JHZ, Liu CY, Sun WY, Duan WJ, Wang G, et al. ALOX15-launched PUFA-phospholipids peroxidation increases the susceptibility of ferroptosis in ischemia-induced myocardial damage. Signal Transduction and Targeted Therapy. 2022; 7: 288. https://doi.org/10.1038/s41392-022-01090-z.
- [39] Jiang C, Shi Q, Yang J, Ren H, Zhang L, Chen S, *et al.* Ceria nanozyme coordination with curcumin for treatment of sepsis-induced cardiac injury by inhibiting ferroptosis and inflammation. Journal of Advanced Research. 2024; 63: 159–170. https://doi.org/10.1016/j.jare.2023.10.011.
- [40] Reina S, Nibali SC, Tomasello MF, Magri A, Messina A, De Pinto V. Voltage Dependent Anion Channel 3 (VDAC3) protects mitochondria from oxidative stress. Redox Biology. 2022; 51: 102264. https://doi.org/10.1016/j.redox.2022.102264.
- [41] Ding Q, Tang W, Li X, Ding Y, Chen X, Cao W, et al. Mitochondrial-targeted brequinar liposome boosted mitochondrial-related ferroptosis for promoting checkpoint blockade immunotherapy in bladder cancer. Journal of Controlled Release: Official Journal of the Controlled Release Society. 2023; 363: 221–234. https://doi.org/10.1016/j.jconrel.2023.09.024
- [42] Martin L, Derwall M, Al Zoubi S, Zechendorf E, Reuter DA, Thiemermann C, et al. The Septic Heart: Current Understanding of Molecular Mechanisms and Clinical Implications. Chest. 2019; 155: 427–437. https://doi.org/10.1016/j.chest.2018.08.
- [43] Bi CF, Liu J, Yang LS, Zhang JF. Research Progress on the Mechanism of Sepsis Induced Myocardial Injury. Journal of Inflammation Research. 2022; 15: 4275–4290. https://doi.org/10. 2147/JIR.S374117.
- [44] Rittig N, Bach E, Thomsen HH, Pedersen SB, Nielsen TS, Jørgensen JO, *et al.* Regulation of Lipolysis and Adipose Tissue Signaling during Acute Endotoxin-Induced Inflammation: A Human Randomized Crossover Trial. PLoS ONE. 2016; 11: e0162167. https://doi.org/10.1371/journal.pone.0162167.
- [45] Güvenç M, Aydin T, Kutlu T, Etyemez M, İşler CT. Tomentosin mitigates the LPS induced cardiac injury by regulating Nrf-2/Nfκβ pathway in mice. European Journal of Pharmacology. 2025; 996: 177589. https://doi.org/10.1016/j.ejphar.2025.177589.
- [46] Lu SM, Yang B, Tan ZB, Wang HJ, Xie JD, Xie MT, et al. TaoHe ChengQi decoction ameliorates sepsis-induced cardiac dysfunction through anti-ferroptosis via the Nrf2 pathway. Phytomedicine: International Journal of Phytotherapy and Phytopharmacology. 2024; 129: 155597. https://doi.org/10.1016/j. phymed.2024.155597.
- [47] Kawaguchi S, Okada M, Ijiri E, Koga D, Watanabe T, Hayashi K, et al. β<sub>3</sub>-Adrenergic receptor blockade reduces mortality in

- endotoxin-induced heart failure by suppressing induced nitric oxide synthase and saving cardiac metabolism. American Journal of Physiology. Heart and Circulatory Physiology. 2020; 318: H283–H294. https://doi.org/10.1152/ajpheart.00108.2019.
- [48] Zhan M, Ding Y, Huang S, Liu Y, Xiao J, Yu H, *et al.* Lysyl oxidase-like 3 restrains mitochondrial ferroptosis to promote liver cancer chemoresistance by stabilizing dihydroorotate dehydrogenase. Nature Communications. 2023; 14: 3123. https://doi.org/10.1038/s41467-023-38753-6.
- [49] Chen X, Kang R, Kroemer G, Tang D. Ferroptosis in infection, inflammation, and immunity. The Journal of Experimental Medicine. 2021; 218: e20210518. https://doi.org/10.1084/jem. 20210518.
- [50] Cui J, Chen Y, Yang Q, Zhao P, Yang M, Wang X, et al. Protosappanin A Protects DOX-Induced Myocardial Injury and Cardiac Dysfunction by Targeting ACSL4/FTH1 Axis-Dependent Ferroptosis. Advanced Science (Weinheim, Baden-Wurttemberg, Germany). 2024; 11: e2310227. https://doi.org/10.1002/advs.202310227.
- [51] Fang X, Wang H, Han D, Xie E, Yang X, Wei J, et al. Ferroptosis as a target for protection against cardiomyopathy. Proceedings of the National Academy of Sciences of the United States of America. 2019; 116: 2672–2680. https://doi.org/10.1073/pnas .1821022116.
- [52] Qiu S, Zhong X, Meng X, Li S, Qian X, Lu H, et al. Mitochondria-localized cGAS suppresses ferroptosis to promote cancer progression. Cell Research. 2023; 33: 299–311. https://doi.org/10.1038/s41422-023-00788-1.
- [53] Sun Y, Yao X, Zhang QJ, Zhu M, Liu ZP, Ci B, et al. Beclin-1-Dependent Autophagy Protects the Heart During Sepsis. Circulation. 2018; 138: 2247–2262. https://doi.org/10.1161/CIRCUL ATIONAHA.117.032821.
- [54] Jakobsson G, Papareddy P, Andersson H, Mulholland M, Bhongir R, Ljungcrantz I, et al. Therapeutic S100A8/A9 blockade inhibits myocardial and systemic inflammation and mitigates sepsis-induced myocardial dysfunction. Critical Care (London, England). 2023; 27: 374. https://doi.org/10.1186/s13054-023-04652-x.
- [55] Peoples JN, Saraf A, Ghazal N, Pham TT, Kwong JQ. Mitochondrial dysfunction and oxidative stress in heart disease. Experimental & Molecular Medicine. 2019; 51: 1–13. https://doi.org/10.1038/s12276-019-0355-7.
- [56] Schenkel LC, Bakovic M. Formation and regulation of mitochondrial membranes. International Journal of Cell Biology. 2014; 2014: 709828. https://doi.org/10.1155/2014/709828.
- [57] Janikiewicz J, Szymański J, Malinska D, Patalas-Krawczyk P, Michalska B, Duszyński J, et al. Mitochondria-associated membranes in aging and senescence: structure, function, and dynamics. Cell Death & Disease. 2018; 9: 332. https://doi.org/10.1038/s41419-017-0105-5.
- [58] Jiang X, Stockwell B R, Conrad M. Ferroptosis: mechanisms, biology and role in disease. Nature Reviews. Molecular Cell Biology. 2021; 22: 266–282. https://doi.org/10.1038/s41580-020-00324-8.
- [59] Du Y, Guo Z. Recent progress in ferroptosis: inducers and inhibitors. Cell Death Discovery. 2022; 8: 501. https://doi.org/10.1038/s41420-022-01297-7.
- [60] She H, Tan L, Du Y, Zhou Y, Guo N, Zhang J, et al. VDAC2 malonylation participates in sepsis-induced myocardial dysfunction via mitochondrial-related ferroptosis. International Journal of Biological Sciences. 2023; 19: 3143–3158. https://doi.org/ 10.7150/ijbs.84613.
- [61] Kim J, Gupta R, Blanco LP, Yang S, Shteinfer-Kuzmine A, Wang K, et al. VDAC oligomers form mitochondrial pores to release mtDNA fragments and promote lupus-like disease. Science (New York, N.Y.). 2019; 366: 1531–1536. https://doi.org/



#### 10.1126/science.aav4011.

- [62] Zhu T, Liu B, Wu D, Xu G, Fan Y. Autophagy Regulates VDAC3 Ubiquitination by FBXW7 to Promote Erastin-Induced Ferroptosis in Acute Lymphoblastic Leukemia. Frontiers in Cell and Developmental Biology. 2021; 9: 740884. https://doi.org/ 10.3389/fcell.2021.740884.
- [63] Luo P, Zhang Q, Shen S, An Y, Yuan L, Wong YK, et al. Mechanistic engineering of celastrol liposomes induces ferroptosis and apoptosis by directly targeting VDAC2 in hepatocellular carcinoma. Asian Journal of Pharmaceutical Sciences. 2023; 18: 100874. https://doi.org/10.1016/j.ajps.2023.100874.
- [64] Xu Y, Tummala SR, Chen X, Vardi N. VDAC in Retinal Health and Disease. Biomolecules. 2024; 14: 654. https://doi.org/10. 3390/biom14060654.
- [65] Yang C, Zhao Y, Wang L, Guo Z, Ma L, Yang R, et al. De novo pyrimidine biosynthetic complexes support cancer cell proliferation and ferroptosis defence. Nature Cell Biology. 2023; 25: 836–847. https://doi.org/10.1038/s41556-023-01146-4.
- [66] Wang F, Min J. DHODH tangoing with GPX4 on the ferroptotic stage. Signal Transduction and Targeted Therapy. 2021; 6: 244. https://doi.org/10.1038/s41392-021-00656-7.

